


Article

The Formation and Modification of the Arcuate Tectonic Belt in the Northeastern Tibetan Plateau: Insight from Three-Dimensional Finite Element Numerical Simulation

Yilin Zhao ^{1,2}, Wei Shi ¹, Yujun Sun ^{1,*}  and Guiting Hou ^{2,*}

¹ SinoProbe Laboratory, Chinese Academy of Geological Sciences, Beijing 100094, China; 18811680869@163.com (Y.Z.); shiweinmg@163.com (W.S.)

² School of Earth and Space Sciences, Peking University, Beijing 100871, China

* Correspondence: sunyujunabc@163.com (Y.S.); gthou@pku.edu.cn (G.H.)

Abstract: The arcuate tectonic belt in the northeast Tibetan Plateau has been a contentious topic regarding its formation and evolution, owing to its distinctive geological structure as the lateral growth boundary of the plateau. In this research, leveraging geological and geophysical data, a three-dimensional finite element numerical model is employed to explore the impact of lateral and vertical inhomogeneities in lithospheric strength on the northeast Tibetan Plateau's growth and the arcuate tectonic belt's formation and alteration. Additionally, the kinematic and deformation traits of the arcuate tectonic belt, such as regional motion velocity, stress, and crustal thickness during shortening and strike-slip deformation, are comparatively analyzed. The findings indicate that the arcuate tectonic belt takes shape when the weakly strengthened Tibetan Plateau is impelled into the Yinchuan Basin after being obstructed by the robust Alax and Ordos blocks during lateral expansion. Intense shear deformation occurs at the block boundaries during the arc tectonic belt's formation. The weak middle-lower crust, serving as a detachment layer, facilitates the plateau's lateral growth and crustal shortening and thickening without perturbing the overall deformation characteristics. It is verified that the arcuate tectonic belt was formed during the NE-SW compression phase from around 9.5 to 2.5 Ma, accompanied by significant crustal shortening and thickening. Since 2.5 Ma, within the ENE-WSW compression process, the internal faults of the arcuate tectonic belt are predominantly strike-slip, with no pronounced crustal shortening and thickening. Only local topographical modification is conspicuous. This study will enhance our comprehension of the Tibetan Plateau's uplift and lateral growth process and furnish a foundation for investigating the formation of arcuate tectonic belts.

Keywords: the northeast Tibetan plateau; arcuate tectonic belt; formation mechanism; plateau growth; finite element numerical simulation



Academic Editor: Antoni Calafat

Received: 4 December 2024

Revised: 2 January 2025

Accepted: 7 January 2025

Published: 18 January 2025

Citation: Zhao, Y.; Shi, W.; Sun, Y.;

Hou, G. The Formation and

Modification of the Arcuate Tectonic

Belt in the Northeastern Tibetan

Plateau: Insight from

Three-Dimensional Finite Element

Numerical Simulation. *J. Mar. Sci. Eng.*

2025, 13, 170. [https://doi.org/](https://doi.org/10.3390/jmse13010170)

10.3390/jmse13010170

Copyright: © 2025 by the authors.

Licensee MDPI, Basel, Switzerland.

This article is an open access article

distributed under the terms and

conditions of the Creative Commons

Attribution (CC BY) license

([https://creativecommons.org/](https://creativecommons.org/licenses/by/4.0/)

[licenses/by/4.0/](https://creativecommons.org/licenses/by/4.0/)).

1. Introduction

Since the continent–continent collision between the Indian plate and the Eurasian plate during the Cenozoic era [1,2], the ceaseless northward migration of the Indian plate has constituted the principal impetus for the uplift and lateral expansion of the Tibetan Plateau [3,4]. In the late Cenozoic, under the governance of deep-seated structures and deformations [5,6], the lateral growth of the Tibetan Plateau was impeded by adjacent blocks (Figure 1), giving rise to a geomorphic boundary belt of complex and diverse structures encircling the plateau [7,8]. The northern and eastern peripheries of the Tibetan

Plateau are typified by abrupt geomorphic belts. The southeastern margin is distinguished by a basin–mountain alternating geomorphic belt that aligns with the expansion trend of the plateau. The northeastern margin exhibits a parallel or arcuate basin–mountain alternating geomorphic zone that is perpendicular to the spreading direction of the plateau, with the topography gradually descending along the spreading direction.

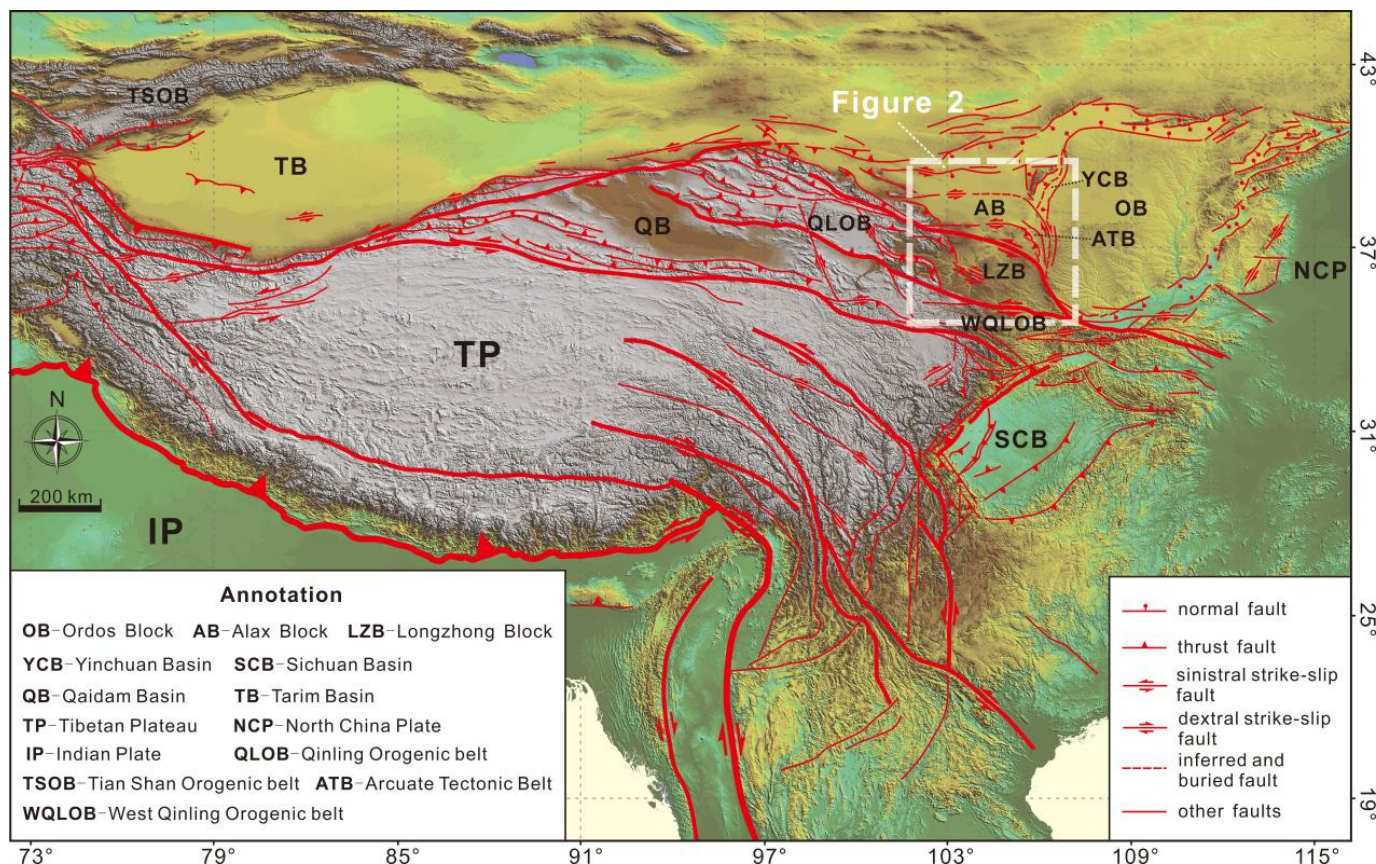


Figure 1. Tectonic geomorphological map of the Tibetan Plateau and its adjacent regions. The fault data were sourced from the Data Sharing Infrastructure of the Seismic Active Fault Survey Data Center, available at <https://www.activefault-datacenter.cn> (accessed on 26 April 2020). The DEM data with a resolution of 90 m was acquired from the Geospatial Data Cloud, accessible at <http://www.gscloud.cn> (accessed on 26 May 2019).

Regionally, the arcuate tectonic belt situated in the northeast of the Tibetan Plateau and the Yinchuan Basin is confined within the triangular zone demarcated by the Alax block, the Ordos block, and the Longzhong block [9]. This triangular area is constituted by Meso-Cenozoic basins [10]. It has been demonstrated that the arcuate tectonic belt is a consequence of intracontinental compressive deformation, and it comprises a sequence of thrust faults and folds that have developed along the frontal portion of the arcuate tectonic belt [11]. Nevertheless, a significant number of field investigations [12–17] and GPS data analyses [18,19] imply that the four principal faults within the arcuate tectonic belt predominantly exhibit the characteristics of strike-slip motion, with only the Liupanshan Fault, located to the south of the arcuate tectonic belt, being characterized by thrusting. Previous research has indicated that the formation mechanism of the arcuate tectonic belt has been a subject of contention, owing to the complexity of the crust–mantle structures and the deformation processes within the study area. Tian and Ding [20], based on the quasi-trijunction structural model, contended that the formation of the arcuate tectonic belt was attributed to the fact that the Tibetan Plateau was impelled into the relatively weak Yinchuan

Basin after being obstructed by the firm Alax and Ordos blocks due to the northeastward expansion of the Tibetan Plateau. This simultaneously instigated the left-lateral strike-slip of the Haiyuan fault zone and the right-lateral strike-slip of the Niushoushan–Luoshan Fault Zone. Wang et al. [21] and Lei et al. [14] proposed that the arcuate tectonic belt represents a “thin-skin” forward thrust structure resulting from the bottom detachment caused by the lateral growth of the plateau. This structure initiates from the Haiyuan Fault and progressively extends towards the northeast. Chen et al. [22] maintained that each fault within the arcuate tectonic belt is characterized by an early stage of thrusting followed by a later stage of strike-slip, with the two stages of deformation successively propagating in the northeastward direction from the Haiyuan Fault. Upon synthesizing the paleotectonic stress field [12] and chronology [23–25], it becomes evident that the arcuate tectonic belt endured significant shortening during the Middle/Late Miocene to Pliocene epoch (around ~9.5–2.58 Ma) under the influence of NE-SW compression. This shortening was responsible for the origination of the arcuate tectonic geomorphological features. In contrast, since the Early Pleistocene (approximately 2.58 Ma), the arcuate tectonic belt, being governed by ENE-WSW compression, has been distinctly characterized by strike-slip. Concurrently, a multitude of Quaternary pull-apart basins have emerged and evolved along the fault zone.

In light of the heterogeneous nature of the strength [26–31] within the arcuate tectonic belt and the evolution of the paleotectonic stress field [12], we employed the three-dimensional finite element numerical model in this study to dissect the crustal shortening phase (~9.5–2.5 Ma) and the strike-slip stage (since 2.5 Ma) of the arcuate tectonic belt. Additionally, we delved into the formation mechanism of the arcuate tectonic belt in conjunction with the crustal deformation and fault activity that occurred during these two distinct stages.

2. Geological and Geophysical Background

2.1. Tectonic Setting

In general, the arcuate tectonic belt is composed of four northeast-protruding arcuate fault zones (as shown in Figure 2). These zones, arranged from south to north, are the Haiyuan fault zone (F_1), the Xiangshan–Tianjingshan fault zone (F_2), the Yantongshan fault zone (F_3), and the Niushoushan–Luoshan fault zone (F_4). Regionally, the belt diverges toward the northwest, converges into the Liupanshan tectonic belt toward the south, and is terminated by the northern margin fault zone of the West Qinling (F_5) to the south [32].

The Haiyuan fault zone represents a pre-existing, extensive, and deep-seated fault zone that penetrates through the Moho, effectively demarcating the Longzhong block in the southern region from the Meso-Cenozoic basins in the north [9]. In terms of fault kinematics, the Haiyuan fault zone is segmented such that the western part is characterized by a strike-slip section, while the eastern part is distinguished by a thrust section, with the Nanhua Shan serving as the dividing line [33]. The Xiangshan–Tianjingshan fault zone, which is delimited by Qingsheya–Shuangerzi, is further divided into its eastern and western parts according to the fault modalities, manifesting the traits of right-lateral en echelon configurations [12]. The westward elongation from Shixia is recognized as the Tianqiaogou–Huangyangchuan fault zone, which is interconnected with the Lenglongling [34,35]. The Yantongshan fault zone surfaces at Yachigou, northeast of Zhongwei City in the north. It traverses the Yellow River to the southeast, extends along the eastern foothills of Yantong Shan and Yao Shan southward, and ultimately combines with the Liupanshan fault zone in the south. Probably, its cutting depth is less than the other three, existing as a basement fault [36,37]. The Niushoushan–Luoshan fault zone, being connected with the Xiaoguanshan fault to its south [13,25], represents the outermost delimiting fault of the northeast Tibetan Plateau. This fault zone also acts as the boundary separating the Tibetan Plateau

from the Ordos block and the Alax block [13]. Moreover, it constitutes a deep-seated fault zone that cuts through the Moho [37,38]. The arcuate tectonic belt has been subject to a complex and intricate tectonic evolution, with a summary presented in Table 1.

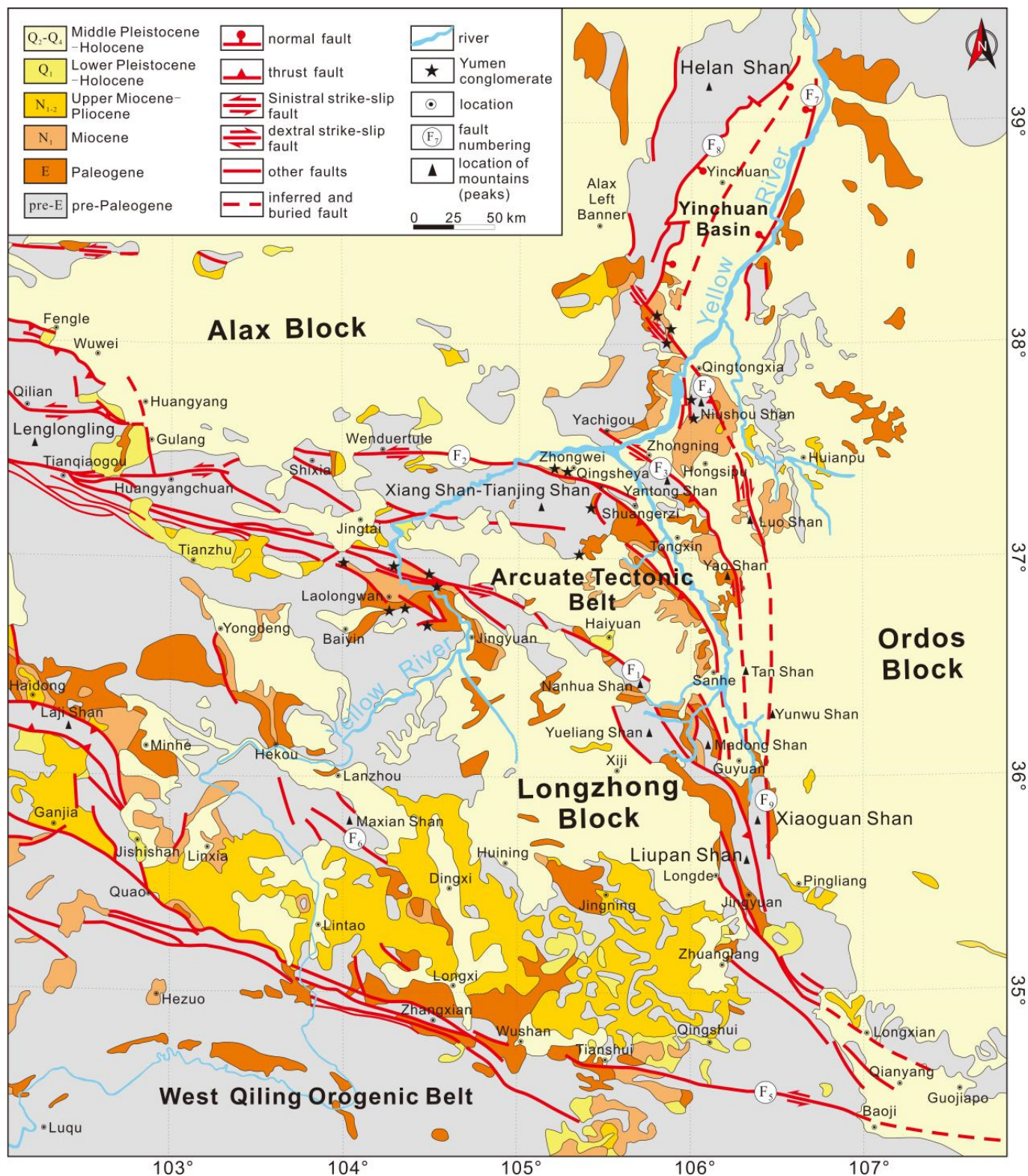


Figure 2. Geological schematic map of the study area. This map has been modified by CorelDRAW (Version 2018) based on [25]. The expanded portion is sourced from the online geological maps of Chinese provinces offered by the OSGeo China Center (<https://www.osgeo.cn/>, accessed on 24 October 2016), which cover Gansu, Qinghai, Shaanxi, the Ningxia Hui Autonomous Region, and

the Inner Mongolia Autonomous Region. F₁: Haiyuan fault zone; F₂: Xiangshan–Tianjingshan fault zone; F₃: Yantongshan fault zone; F₄: Niushoushan–Luoshan fault zone; F₅: the fault of the northern margin of the West Qinling Mountains; F₆: Maxianshan fault zone; F₇: Yellow River fault; F₈: the fault at the east piedmont of Helan Shan; F₉: Xiaoguanshan fault.

Table 1. The tectonic evolution of the arcuate tectonic belt.

| Fault | Initial Age Ma | Maximum Horizontal Compression | Tectonic Event | Fault Mechanism | References |
|----------------|-------------------|--------------------------------------|------------------------|---|------------|
| F ₁ | ~9.5 | NE-SW | thrust | thrust | [12,14,21] |
| | 5.4 | ENE-WSW | thrust and strike-slip | thrust and sinistral strike-slip | |
| | 2.6 | | strike-slip | sinistral strike-slip (west); thrust and sinistral strike-slip (east) | |
| F ₂ | 5.4 | NE-SW | thrust | thrust and sinistral strike-slip | [14,21] |
| | ~2.7 | ENE-WSW | strike-slip | normal-sinistral strike-slip (west); thrust and sinistral strike-slip (east) | |
| F ₃ | 5.4 or ~2.7 | NE-SW or ENE-WSW | thrust | thrust and dextral strike-slip | [13,14,21] |
| F ₄ | ~2.5 | NW-SE | thrust and strike-slip | thrust and sinistral strike-slip | [14,17,39] |
| | 0.15 | NNE-SSW | strike-slip | dextral strike-slip | |

Note: The initial age of the Yantongshan fault zone (F₃) has not been accurately determined.

2.2. Distribution Characteristics of Crustal Thickness and Rheological Strength

In Figure 3, the crustal thickness contour map sourced from the CRUST 1.0 model [40,41] is superimposed upon the surface geomorphology and major faults, thus revealing the interrelationships between the structure, crustal deformation, and geomorphic features. The Alax block demonstrates stable structural traits, with the Moho surface depth decreasing steadily from west to east. The Ordos block is typified by a steady crustal structure and negligible Moho undulations. The Yinchuan Basin is flanked by the Yellow River fault (F₇) on the east and the east piedmont fault of the Helan Shan (F₈) on the west, wherein the Yellow River fault penetrates the Moho [42–44]. The crust–mantle architecture of the Yinchuan Basin is shallower at the peripheries and deeper in the central region [42]. The arcuate tectonic belt, along with the Yinchuan Basin, composes the Meso-Cenozoic basins in the northeastern Tibetan Plateau, renowned for its vigorous activity and recurrent earthquakes along the boundary faults [9,45]. The Moho depth tapers off gradually from the southwest to the northeast, with especially prominent disparities observable in the boundary fault zones [38,46]. The Longzhong block, demarcated by the northern margin fault of the West Qinling fault (F₅), the Maxianshan fault (F₆), and the Haiyuan fault (F₁), is likewise a stable entity. Its Moho progressively dips eastward, attaining its greatest depth beneath Liupan Shan and Xiaoguan Shan, before shallowing again within the Ordos block [45]. The rheological potency of a block can be gauged by the velocity signatures of P-waves and S-waves. Reduced seismic velocities may signify a less robust rheological strength, and vice versa [9,46,47].

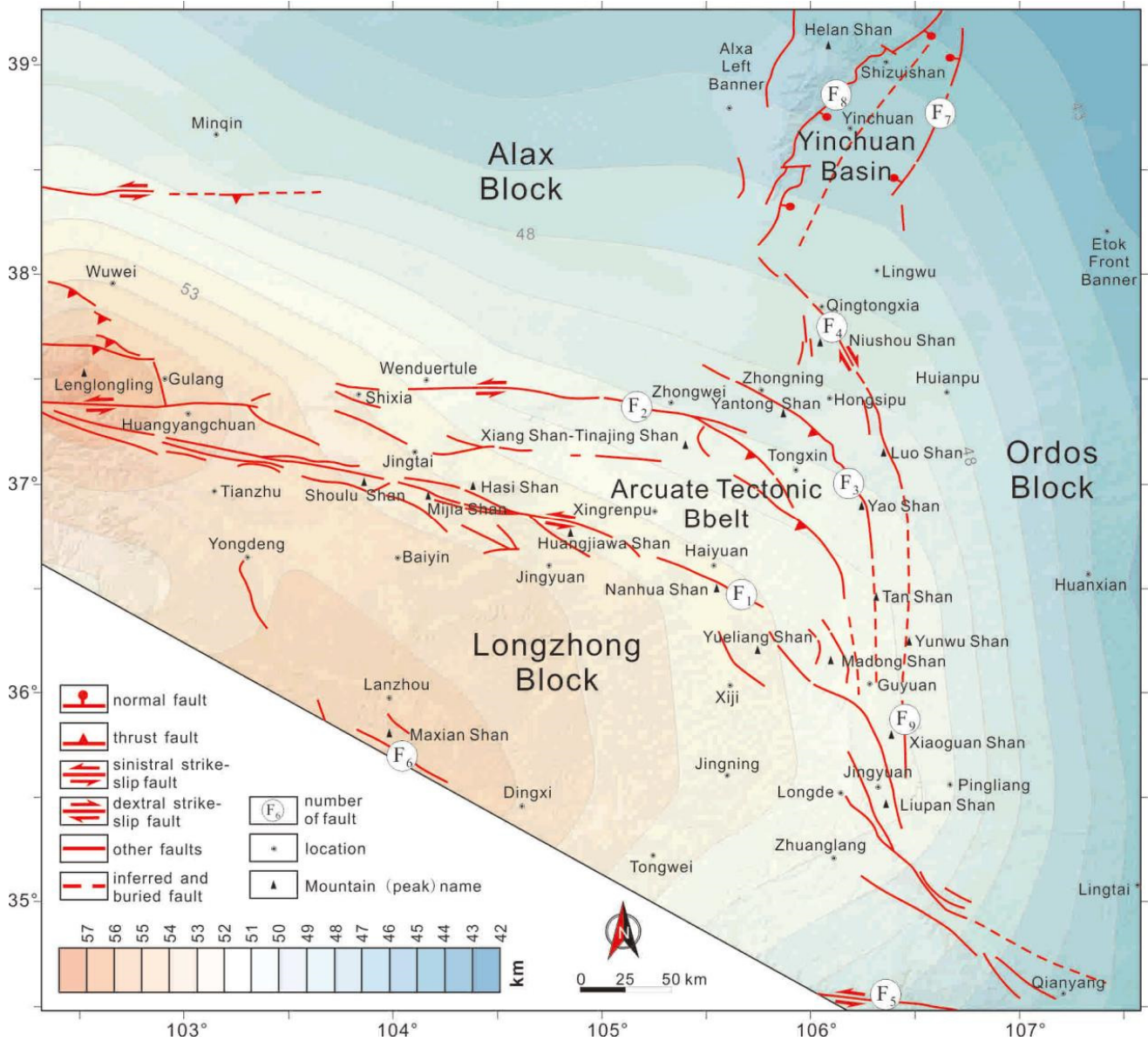


Figure 3. Tectonic geomorphological features and crustal thickness distribution within the study region. The data pertaining to the crustal thickness is obtained from the publicly accessible CRUST 1.0 model, available at the website: <https://igppweb.ucsd.edu/~gabi/crust1.html> (accessed on 27 August 2013).

3. Numerical Model

3.1. Governing Equation

Elastic constitutive equations are usually utilized to study the short-term deformation of the crust or lithosphere [48,49]. However, in order to describe large-scale, long-term deformation, the continental lithosphere can be viewed as a continuum, following Newtonian fluids or power-law fluids [50–55]. In this study, the constitutive relation of viscous fluid is adopted. In order to account for the inhomogeneity of the medium, different blocks are assigned with different equivalent viscosity coefficients. Within the three-dimensional space, the momentum conservation equation used to describe a quasi-static incompressible viscous fluid is

$$-\frac{\partial P}{\partial x_j} + \frac{\partial}{\partial x_i} \left(\eta_{eff} \frac{\partial v_j}{\partial x_i} \right) + \rho g_i = 0 \quad j = 1, 2, 3 \quad (1)$$

Mass conservation equation (incompressible condition):

$$\frac{\partial v_j}{\partial x_j} = 0 \quad (2)$$

where P is the pressure, v_j is the velocity component, η_{eff} is the effective viscosity, ρ is the density, and $g_j = [0, 0, g]^T$ is the acceleration of gravity. The constitutive equation is as follows:

$$\sigma_{ij} = -P\delta_{ij} + 2\eta_{eff}\dot{\epsilon}_{ij} \quad (3)$$

where σ_{ij} is the stress tensor (take as negative in compression), and δ_{ij} is the Kronecker delta tensor. The strain rate tensor $\dot{\epsilon}_{ij}$ is

$$\dot{\epsilon}_{ij} = \frac{1}{2} \left(\frac{\partial v_i}{\partial x_j} + \frac{\partial v_j}{\partial x_i} \right) \quad (4)$$

In this study, the three-dimensional viscous large deformation finite element simulation program developed by Sun et al. [56] was used to solve the above equations. The program verified the reliability [57] of the numerical calculation by comparing it with the sandbox experiment [58] and the sinking of a rectangular block with a different viscosity contrast between the sinking block and its surrounding weak medium [59].

3.2. Finite Element Model and Boundary Conditions

In the horizontal plane, the three-dimensional finite element model is partitioned into four segments: the Ordos block (OB), the Alax block (AB), the Longzhong block (LZB), and the Meso-Cenozoic basins (M-CB). The demarcation between the Longzhong block and the other three regions is marked by the Haiyuan fault zone (F_1). The planar contour of the model takes the form of a pentagon, which is derived by truncating the lower left corner of a quadrilateral (as depicted in Figure 4a,b). The five vertex coordinates are A (102.3157° E, 39.26847° N), B (107.5843° E, 39.26847° N), C (107.5843° E, 34.47701° N), D (106.1083° E, 34.47701° N), and E (102.3157° E, 36.59635° N), respectively. Point F (102.3157° E, 37.38174° N) serves as the boundary point along the AE edge, with disparate boundary conditions prevailing on either side. Free-slip boundary conditions are imposed along AF, AB, and BC, while velocity boundary conditions are applied to EF, CD, and DE. The magnitude and orientation of the velocities are subject to temporal variation. The vertical extent of the model measures 100 km, and the meshing configuration is illustrated in Figure 4c.

To validate the disparity in lithospheric deformation during the early thrusting and subsequent strike-slip, the overall simulation calculation duration is set at 9.5 Ma. The transition time is designated as 2.5 Ma, signifying the commencement of strike-slipping in the northeastern Tibetan Plateau. Given that the calculation time step is 0.1 Ma, the thrusting deformation spanning from 9.5 to 2.5 Ma corresponds to steps 0–70 (as shown in Figure 4a), and the strike-slip from 2.5 Ma to the present correlates with steps 71–95 (depicted in Figure 4b). In the model, it is postulated that the boundary conditions remain uniform in the vertical direction. During the thrust stage, the velocity direction applied to the EF, CD, and DE edges is uniformly set to N45° E. The velocity along the DE edge is constantly 3.87 mm/yr, while the velocities along the EF and CD sides diminish linearly from 3.87 mm/yr to 0. In the strike-slip stage, the velocity of the EF edge is oriented at N70° E and decreases linearly from 3.87 mm/yr to 0. The velocity magnitude imposed on the DE edge is 3.87 mm/yr, and its direction, from point E to point D, varies linearly from N70° E to 90° in accordance with the horizontal coordinate. The direction and magnitude of the velocity on the CD side also change linearly with the horizontal coordinate. The velocity directions shift from 90° S to 110° E, and the magnitudes decline from 3.87 mm/yr to 0.

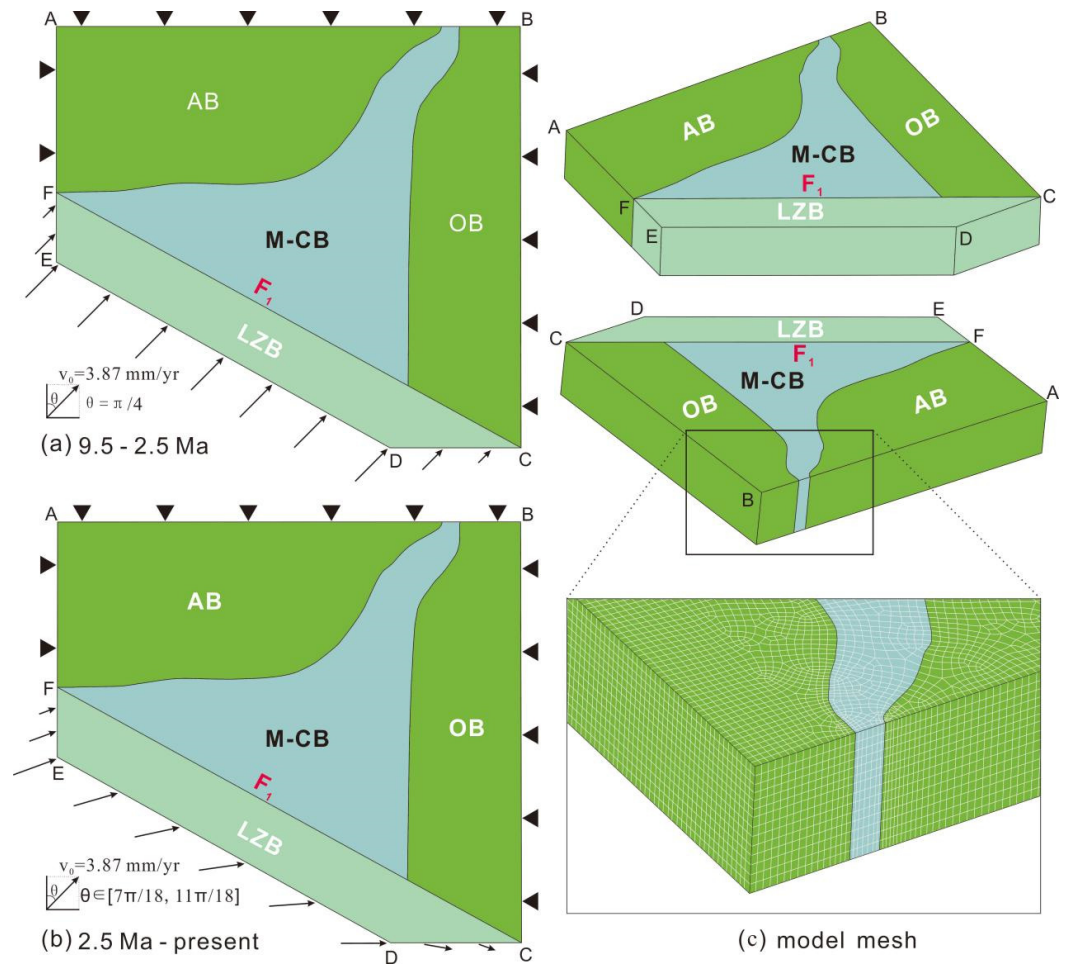


Figure 4. Block division, boundary conditions and mesh division within the numerical model. (a) Illustrated are the boundary conditions during the period from 9.5 Ma to 2.5 Ma. (b) Presented are the boundary conditions from 2.5 Ma up to the present. (c) Shown is the model mesh division with a rotation angle of 0.05 degrees. The black arrow symbolizes the velocity boundary conditions, and the black triangle represents the free-slip boundary conditions. Here, θ denotes the azimuth of the velocity. OB: Ordos block; AB: Alax block; LZB: Longzhong block; M-CB: Meso-Cenozoic basins (including the arcuate tectonic belt and Yinchuan Basin); F_1 : Haiyuan fault zone.

3.3. Model Parameters

The lithospheric strength in the northeastern margin of the Tibetan Plateau is heterogeneous [29,30,60–62]. Firstly, the Ordos and Alax blocks are stable cratonic blocks possessing relatively high lithospheric strength. In contrast, the Meso-Cenozoic basins have been disrupted by multi-stage tectonic activities, leading to a relatively weak lithospheric strength. The lithospheric strength of the Longzhong block is weaker than that of the Ordos and Alax blocks but stronger than that of the Meso-Cenozoic basins. Secondly, the Longzhong block and the Meso-Cenozoic basins have a relatively weak lower or middle-lower crust compared to the Ordos and Alax blocks.

Plastic deformation was not taken into account in this study. Consequently, the parameters involved in the numerical simulation include effective viscosity (η_{eff}) and density (ρ). Viscosity serves as an indicator of lithospheric strength. To assess the impacts of lateral viscosity differences on lithospheric deformation, five models were devised (Table 2). To evaluate the effects of vertical viscosity differences on lithospheric deformation, three models were designed (Table 3).

Table 2. Parameters for Case–1 to Case–5.

| Block | Case–1 η_{eff} (Pa·s) | Case–2 η_{eff} (Pa·s) | Case–3 η_{eff} (Pa·s) | Case–4 η_{eff} (Pa·s) | Case–5 η_{eff} (Pa·s) |
|-----------|-------------------------------|-------------------------------|-------------------------------|-------------------------------|-------------------------------|
| OB and AB | 1×10^{23} | 1×10^{23} | 1×10^{23} | 1×10^{23} | 1×10^{23} |
| M-CB | 1×10^{23} | 5×10^{22} | 2.5×10^{22} | 1×10^{22} | 2.5×10^{22} |
| LZB | 1×10^{23} | 5×10^{22} | 2.5×10^{22} | 1×10^{22} | 5×10^{22} |

Note: The upper crust density is 2700 kg/m³, middle crust 2800 kg/m³, lower crust 3000 kg/m³, and lithospheric mantle 3300 kg/m³.

Table 3. Parameters for Case–6 to Case–8.

| Block | Layer | Case–6 η_{eff} (Pa·s) | Case–7 η_{eff} (Pa·s) | Case–8 η_{eff} (Pa·s) |
|-----------|-------|-------------------------------|-------------------------------|-------------------------------|
| OB and AB | UC | 1×10^{23} | 1×10^{23} | 1×10^{23} |
| | MC | 1×10^{23} | 1×10^{23} | 1×10^{23} |
| | LC | 1×10^{23} | 1×10^{23} | 1×10^{23} |
| | LM | 1×10^{23} | 1×10^{23} | 1×10^{23} |
| M-CB | UC | 2.5×10^{22} | 2.5×10^{22} | 2.5×10^{22} |
| | MC | 2.5×10^{22} | 2.5×10^{22} | 7.5×10^{21} |
| | LC | 7.5×10^{21} | 7.5×10^{20} | 7.5×10^{20} |
| | LM | 2.5×10^{22} | 2.5×10^{22} | 2.5×10^{22} |
| LZB | UC | 5×10^{22} | 5×10^{22} | 5×10^{22} |
| | MC | 5×10^{22} | 5×10^{22} | 5×10^{21} |
| | LC | 5×10^{21} | 5×10^{20} | 5×10^{20} |
| | LM | 5×10^{22} | 5×10^{22} | 5×10^{22} |

Note: Refer to Table 2 for lithospheric layer density settings. UC: upper crust; MC: middle crust; LC: lower crust; LM: lithospheric mantle.

To streamline the model, the Ordos and Alax blocks are considered as the same material with the viscosity set at 1×10^{23} Pa·s. Case–1 represents a homogeneous model composed of a single material, where the viscosity of all blocks is configured as 1×10^{23} Pa·s. To account for the impact of lithospheric strength heterogeneity on the formation of the arcuate tectonic belt, in Case–2 through Case–4, the Meso-Cenozoic basins and the Longzhong block are treated as the same material. Their viscosities are set to 5×10^{22} Pa·s, 2.5×10^{22} Pa·s, and 1×10^{22} Pa·s, respectively. Case–5 is a model designed for comparing three materials, taking into consideration the distinctions between the Longzhong block and the other blocks. To evaluate the influence of the vertical heterogeneity in lithospheric strength on the formation of the arcuate tectonic belt during the thrust stage (9.5–2.5 Ma), we developed Case–6 through Case–8 based on Case–5. In Case–6 and Case–7, the Longzhong block and the Meso-Cenozoic basins possess a weakened lower crust. The lower crustal viscosity in Case–7 is one order of magnitude lower than that in Case–6 (as shown in Table 3). In Case–8, the Longzhong block and the Meso-Cenozoic basins have a weakened middle-lower crust. The viscosity of the lower crust is 0.1 times that of the middle crust (refer to Table 3).

4. Results

All the calculated results in this study were plotted by Surfer (Version 11.0) and MATLAB (Version R2020b), and further refined by CorelDRAW (Version 2018).

4.1. Impact of Horizontal Strength Variation on Arcuate Tectonic Belt Formation

In Case–1, with homogeneous materials and no lithospheric strength difference, the model’s horizontal velocity uniformly decreases northeastward without abrupt changes (Figure 5a). The Meso-Cenozoic basins lack a convex-to-northeast oroclinal structure, and there is no squeezing of the Longzhong block into the Yinchuan Basin along the Ordos-

Alax block boundary. However, uplift rates are higher in the southwest and southeast corners than in the northwest and northeast corners, with the highest rate in the southeast and negative vertical velocities in the northwest and northeast. As a transition zone, the lithospheric strength of the Longzhong block and the Meso-Cenozoic basins significantly impacts deformation. We examined the effect of their viscosity on lithospheric deformation in Case-2–Case-4 (Figure 5b–d). The results indicate that as their viscosity decreases, both horizontal and vertical velocities in the region increase. When their viscosity is 0.25 times or less than that of Alax and Ordos, the vertical velocity gradient bands align with the present-day arc tectonic belt location (Figure 5c,d).

Case-5 exhibits two deformation phases. The initial stage is the thrust stage, governed by NE-SW compression from approximately 9.5–2.5 Ma (Figure 5e). The subsequent stage is the strike-slip stage, controlled by ENE-WSW compression since 2.5 Ma (Figure 5f). In Case-5, the impact of three block strength types on the arcuate tectonic belt formation during the extrusion stage is considered (Figure 5e). The degree of arc compression in the vertical velocity of Case-5 is nearly identical to that in Case-3 or Case-4. This implies that the formation of the arcuate tectonic belt is chiefly reliant on the lithospheric strength of the Meso-Cenozoic basins and the Longzhong block.

4.2. Effect of the Directional Change in Block Convergence Velocity on Crustal Thickness and Stress Field

The analysis of the maximum and minimum principal stresses and maximum shear stress during the shortening stage reveals that intense shear deformation predominantly occurs at block boundaries, as depicted in Figure 6a. The Haiyuan fault zone exhibits left-lateral strike-slip activity along its western segment (west of Haiyuan city) and mainly thrusts northeastward with a sinistral strike-slip component along its eastern segment (east of Haiyuan). Concurrently, NW-SE extension takes place in this area. In the Meso-Cenozoic basins, there are three principal areas with high uplift rates (Figures 5e and 7a). The first lies west of Jingtai, between the Xiangshan–Tianjingshan fault zone and the Haiyuan fault zone. The second is south of the Haiyuan fault zone and west of Yongdeng. The third is in the Liupanshan area, with uplift rates of 0.9–1.1 mm/yr, 1.7–1.9 mm/yr, and 0.9–2 mm/yr, respectively, generally decreasing from south to north. The corresponding crustal thicknesses are 44–44.5 km, 44–46.5 km, and 44.5–46.5 km. In the arcuate tectonic belt, uplift rates gradually decline from 0.9 mm/yr in the south to 0 in the Yinchuan Basin, and crustal thicknesses decrease from 45 km in the south to 42 km in the Yinchuan Basin. The Longzhong block is squeezed northeastward along the Ordos and Alax blocks, with its southern margin showing relatively high uplift rates of 1.1–1.4 mm/yr, corresponding to a crustal thickness of 43.5–44.5 km. The uplift rates of the Ordos block range from –0.3 to 1.4 mm/yr, increasing from north to south, with the crust thickness of the northern part being 40 km and gradually thickening to 44.5 km in the south. The Alax block has relatively low uplift rates, ranging from –0.3 to 0.5 mm/yr. From the east to the west, the vertical velocities extend in the NNE-SSW direction and diminish progressively. In contrast, from the north to the south, the vertical velocities spread nearly in the E-W direction and increase correspondingly. The crustal thickness of the Alax block ranges from 40 to 42.5 km, exhibiting a pattern similar to that of the vertical velocity. The central region of the Longzhong block has a relatively low uplift rate of 0.6 mm/yr, and its crustal thickness is 42–44 km, which is marginally thinner than the 45 km obtained through geophysical observations [38,63].

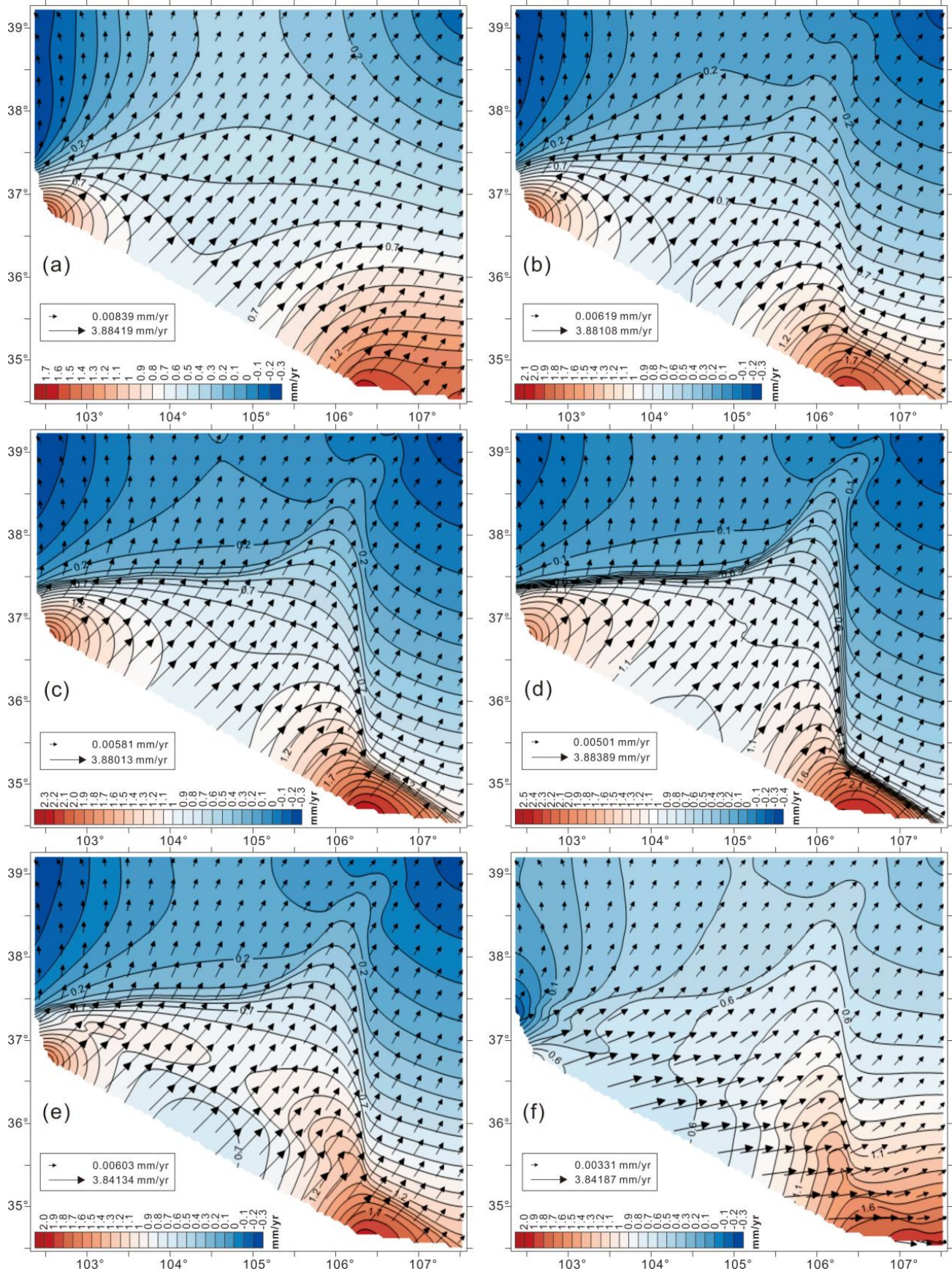


Figure 5. Horizontal velocity (indicated by black arrows) and the contour map of vertical velocity (positive for upward) for Case-1 to Case-5. (a–d) Results of Case-1 to Case-4 at 2.5 Ma. (e) Result of Case-5 at 2.5 Ma. (f) Result of Case-5 at present.

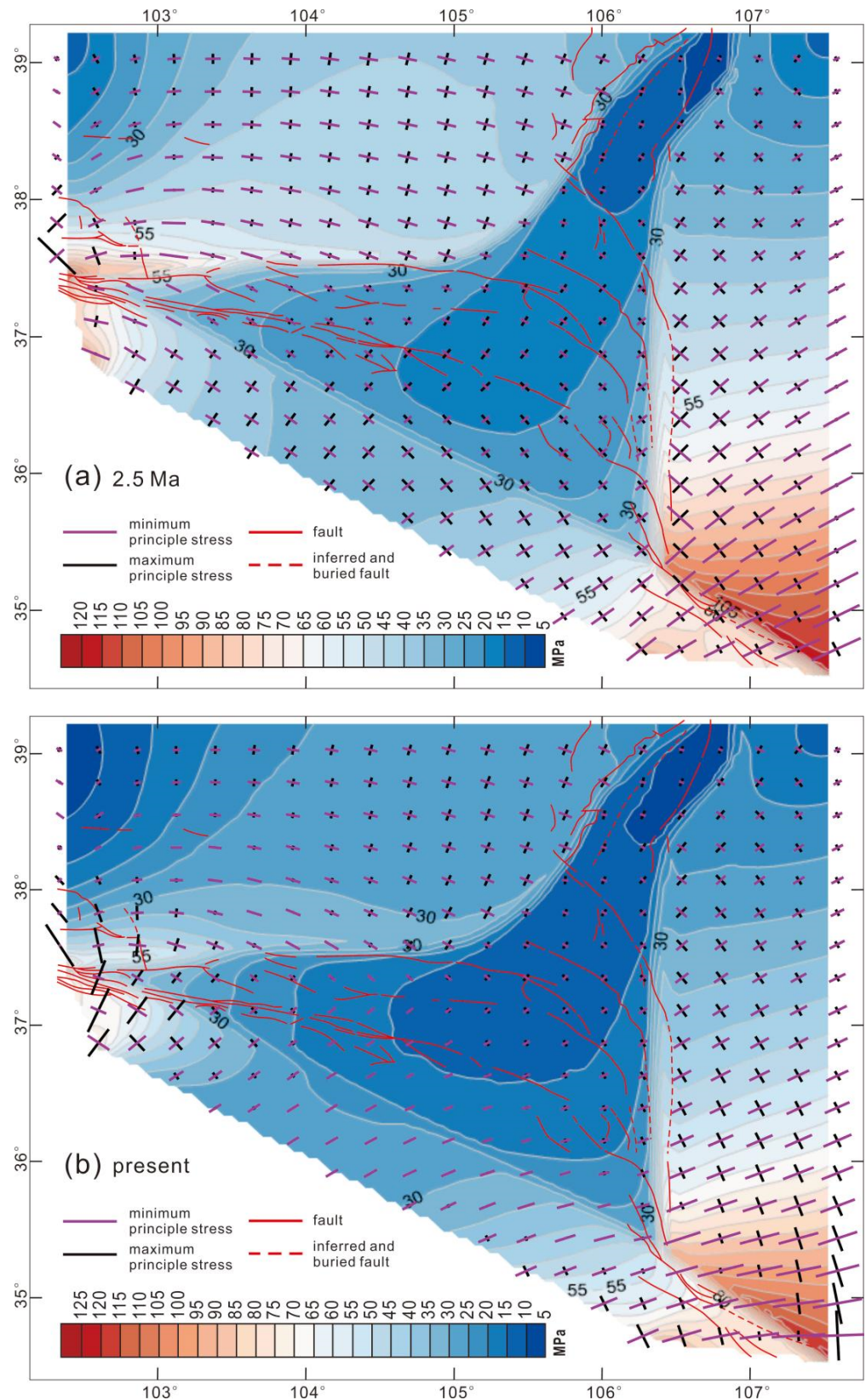


Figure 6. The maximum and minimum principal stresses and the maximum shear stress (shown by contour lines) in Case-5. (a) Results of the thrusting stage (at 2.5 Ma). (b) Results of the strike-slipping stage (at present). In elasticity, we define the tensile stress as positive and the compressive stress as negative. The purple lines indicate the direction and the absolute value of minimum principal stress (representing the maximum compressive stress), and the black lines represent the direction and the absolute value of maximum principal stress.

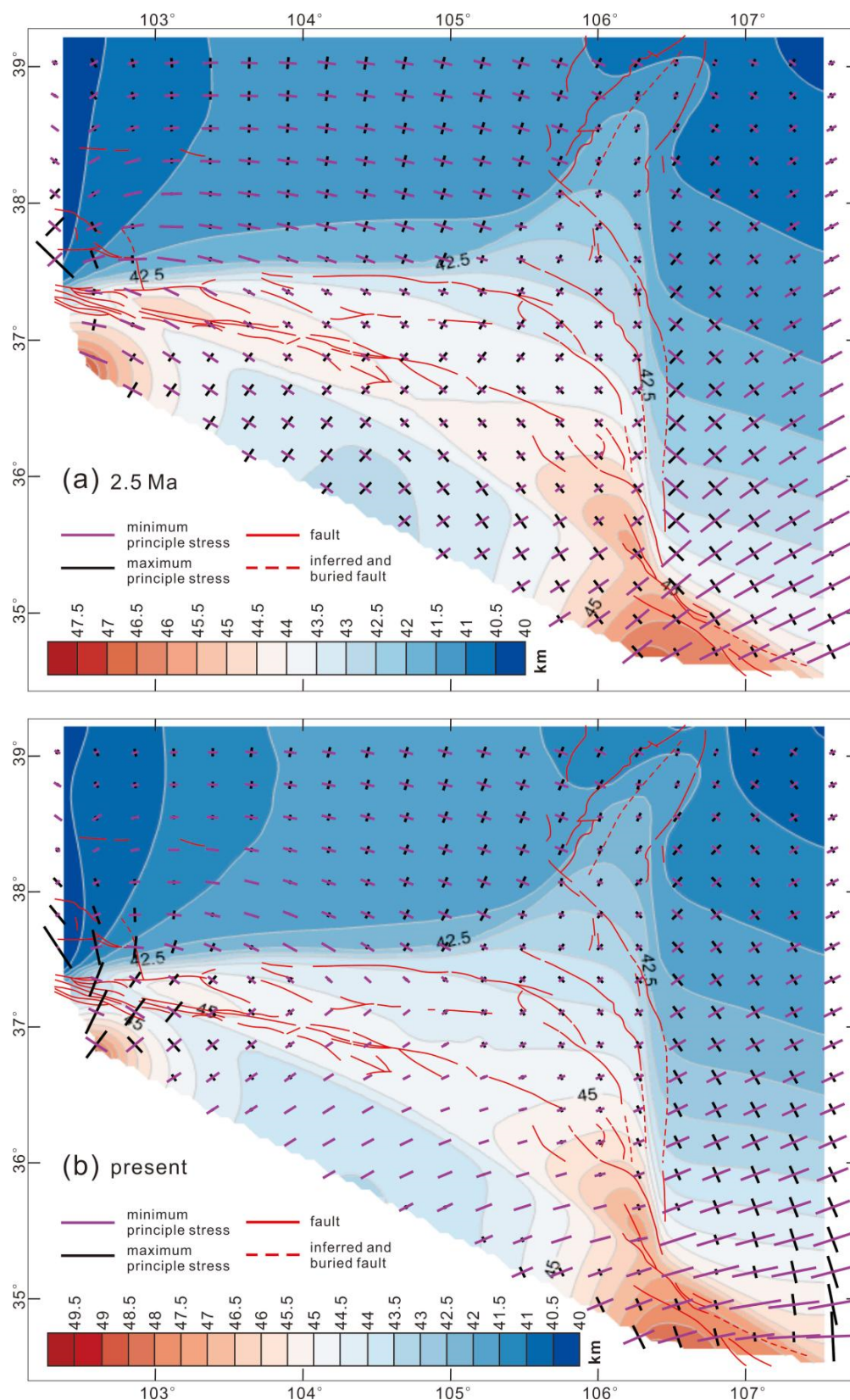


Figure 7. The crustal thickness and the distribution of the maximum and minimum principal stresses in Case-5 during the (a) extrusion stage (2.5 Ma) and (b) strike-slip stage (present).

During the strike-slip stage, the horizontal velocity towards ENE shifts to NE in the northern part of the Haiyuan fault zone and rapidly decreases towards the Yinchuan Basin, as illustrated in Figure 5f. At this moment, the velocity at which the Meso-Cenozoic basins

are squeezing into the Yinchuan Basin begins to decelerate compared to that in the thrust stage (Figure 5e). Figure 6b indicates that the intense shear deformation during the strike-slip stage still takes place at the block boundary but starts to weaken in contrast to the thrust stage. The western region of Jingtai, located between the Xiangshan–Tianjingshan fault zone and the Haiyuan fault zone, as well as the western area of Yongdeng and the southern part of the Haiyuan fault zone, is under the control of WNW-ESE compression and extends in the NNE-SSW direction. Towards the east, the compression direction in the Liupan Shan gradually changes from NE-SW to ENE-WSW, and the extension becomes correspondingly stronger in the NNW-SSE direction. The western segment of the Haiyuan fault zone is marked by normal faulting with a sinistral strike-slip component, while the central segment is dominated by sinistral strike-slip movement and thrust faulting. In contrast, the Liupan Shan area is mainly subjected to nearly E-W compression, accompanied by local extension in the NNW-SSE direction. However, the vertical velocity (Figure 5f) and crustal thickness (Figure 7b) during the strike-slip stage reveal that there is a shortening uplift area in the Liupan Shan area, with uplift rates ranging from 1.1 to 2 mm/yr and a crust thickness of 45.5–49.5 km. The uplift rates in the area west of Jingtai and between the Xiangshan–Tianjingshan fault zone and the Haiyuan fault zone are relatively low, varying from 0.2 to 0.5 mm/yr. The uplift rates in the area west of Yongdeng and the southern part of the Haiyuan fault zone are likewise relatively low, ranging from 0.6 to 0.9 mm/yr. Towards the east, the uplift rates gradually increase. The crust thickness in the Liupan Shan area is 44.5–46 km, and that in the area south of the Haiyuan fault zone and west of Yongdeng is also 44.5–49.5 km. The uplift rates within the arcuate tectonic belt range from 0.5 mm/yr to 1.6 mm/yr, and the crustal thickness varies from 42.5 km to 48.5 km. All these parameters tend to decline from the Liupan Shan area towards the Yinchuan Basin and the west of Jingtai. The vertical velocity contour of the Ordos block extends in an E-W direction. The uplift rate is 0.3 mm/yr in the north and gradually increases to 1.7 mm/yr in the south. The crust of the Ordos block thickens from 40 km in the north to 46 km in the south, with its contour lines spreading in the WNW-ESE direction. The contour lines of the velocity of the Alax block extend from east to west in the N-S direction and the value decreases from 0.4 mm/yr to 0. The crustal thickness of the Alax block gradually decreases from 41 km in the central part to 40 km in the west and to 40.5 km in the eastern part of the Helan Shan. The uplift rates of the Longzhong block increase from 0.5 mm/yr in the west to 2 mm/yr in the east. The middle crust of the Longzhong block is the thinnest, having a thickness of 43.5–45 km, and it thickens gradually towards the east and west.

In conclusion, around 2.5 Ma, there was a crucial temporal boundary for the formation and subsequent modification of the arcuate tectonic belt. During the shortening stage, the Haiyuan fault zone was compressed in the NE-SW direction. Its eastern part was dominated by northeastward thrusting accompanied by a sinistral strike-slip component, while the western part was mainly characterized by sinistral strike-slip. At this point, the arcuate tectonic belt was fundamentally formed. The topography and crustal thickness decreased gradually from the southwest to the northeast. Strong sinistral shear took place at the southeastern boundary of the Alax block, and dextral shear and compression dominated the western and southwestern margins of the Ordos block, respectively. In the strike-slip stage, sinistral strike-slip activity occurred throughout the Haiyuan fault zone, and eastward thrusting happened in the Liupan Shan area, which became the sole rapidly uplifting area within the model. Comparing the crustal thickness between the extrusion stage and the strike-slip stage reveals that the crustal shortening, thickening, and uplifting of the arcuate tectonic belt mainly occur during the thrust stage. The strike-slip stage is governed by strike-slip faulting, and crustal thickening is not conspicuous. The crustal thickness of the

Haiyuan fault zone changes abruptly from the Longzhong block to the Alax block, which aligns with seismic tomography imaging [38,46].

4.3. Impact of Vertical Strength Variation on Arcuate Tectonic Belt Formation

Similar to Case-1–Case-5, to directly reflect the impact of vertical viscosity differences on the development of the arcuate tectonic belt, this paper combined the east-bound velocity u and north-bound velocity v in the results of Case-6–Case-8 into a horizontal velocity and superimposed the contour map of the vertical velocity beneath it. This vertical velocity reflects the uplift rates at different locations within the study area (Figure 8a,c,e). Meanwhile, to explore the influence of vertical viscosity differences on crustal shortening and thickening, the distribution characteristics of crustal thickness in each case are also presented correspondingly (Figure 8b,d,f).

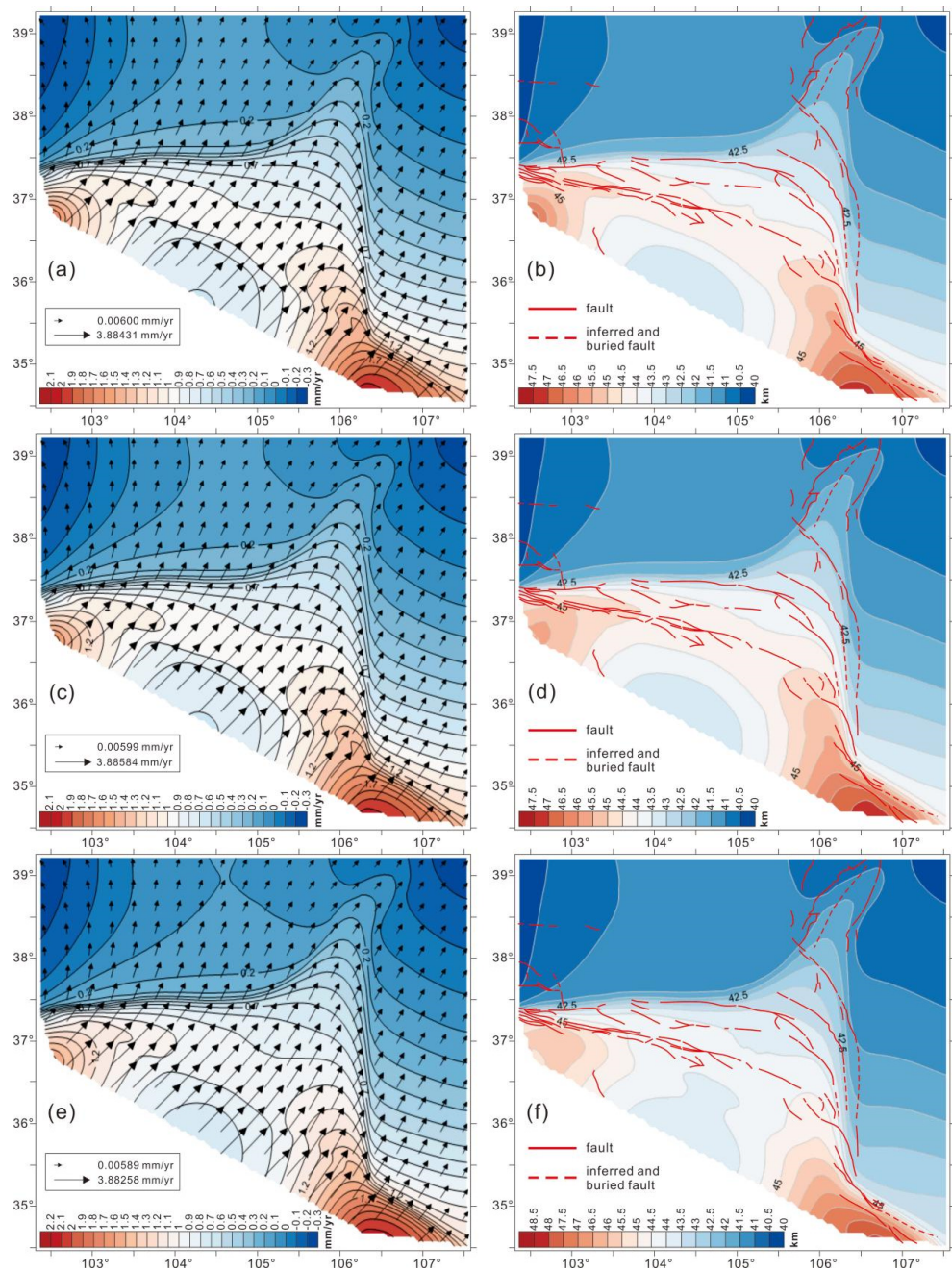


Figure 8. Horizontal velocities and vertical velocity contour maps for Case-6 (a), Case-7 (c), Case-8 (e), and crustal thickness contour maps for Case-6 (b), Case-7 (d), Case-8 (f) at the thrust stage (2.5 Ma).

During the shortening stage of Case-5, the maximum vertical velocity is 2.0 mm/yr and the maximum crust thickness is 47.5 km, as depicted in Figure 5e. In Case-6 and Case-7, the maximum vertical velocity is 2.1 mm/yr (Figure 8a,c), and the maximum crust thickness is also 47.5 km (Figure 8b,d). However, compared with Case-6, the velocity in Case-7 is not as significant in Figure 8c, with a value of 1.1 mm/yr. In Case-8, the maximum vertical velocity is 2.2 mm/yr (Figure 8e) and the maximum crust thickness is 48.5 km (Figure 8f).

Through contrasting the shortening stages of Case-6, Case-7, and Case-5, our findings reveal that a weaker lower crust facilitates the extrusion of crustal materials from the northeastern margin of the Tibetan Plateau into the Yinchuan Basin. Meanwhile, the lower the viscosity of the lower crust, the more conducive it is to the lateral growth of the plateau and the formation of the arcuate tectonic belt. However, when compared with Case-7, if we modify the lower crustal viscosity of the Longzhong block and the Meso-Cenozoic basins, the lateral growth of the plateau is not pronounced, with only a one order of magnitude difference being notable.

By comparing the vertical velocity of Case-6–Case-8 (Figure 8a,c,e), we observe that on the premise of having a weak lower crust in the Longzhong block and the Meso-Cenozoic basins, significant uplift occurs in the Liupan Shan area, as well as in the area west of Jingtai and between the Xiangshan–Tianjingshan fault zone and the Haiyuan fault zone when a weak middle crust is incorporated into the model (Figure 8e). Compared to Case-6 and Case-7, the contour map of the uplift rate in Case-8 indicates that the squeezing trend of isolines into the Yinchuan Basin is more conspicuous.

By comparing the shortening stage of Case-5 with those of Case-6–Case-8, we discover that a weaker lower crust promotes the lateral growth of the plateau and the formation of the arcuate tectonic belt in the northeastern Tibetan Plateau. Nevertheless, vertical crust thickening is not significant when only a weak lower crust is present in the model. Due to the addition of a weak middle crust, the lateral growth of the plateau and the crustal shortening and thickening of the arc tectonic belt are significantly enhanced. Hence, the weak middle crust, similar to the lower crust, likely plays an important role in the lateral growth of the Tibetan Plateau and the formation of the arcuate tectonic belt.

5. Discussion

5.1. Formation of the Arcuate Tectonic Belt and the Horizontal Heterogeneity of Lithospheric Strength

Previous studies have demonstrated that the outward expansion of the Tibetan Plateau can result in diverse deformation patterns due to variations in the rheological strength of the surrounding terranes [61,62]. For instance, the eastern and northern boundaries of the plateau are blocked by the high-strength Sichuan Basin and the Tarim Basin, respectively, leading to steep landforms and concentrated crustal deformation. In contrast, at the northeastern boundaries of the plateau, where multiple blocks are spliced together, there is a gradual topography and diffuse crustal deformation [62]. The findings in this paper further verify that when the rheologies of multiple blocks on the northeastern margin of the Tibetan Plateau differ, more complex deformation patterns, like arcuate tectonic belts, will form. Our study results reveal that when the rheological strength of the Yinchuan Basin located between the Ordos and Alax blocks is low, the high strain during the lateral growth of the plateau is mainly distributed within the Yinchuan Basin (Figure 5c–e). The transition boundary between the Tibetan Plateau with low rheological strength and the Ordos and Alax blocks with high rheological strength serves as a major area for fault development and crustal thickening (Figure 7). Moreover, our rheological structure is based on the effective viscosity (Figure 9) derived from the thermal model [63], which is similar to the

thermal structure shown by the updated global heat flow data set [64]. We assume that the rheological structure reflected by effective viscosity has not changed significantly since the late Cenozoic. The calculated rheological structure and deformation characteristics are consistent with the deep structure observed through geophysics [9,45,65] and the surface deformation observed in the field [12–18].

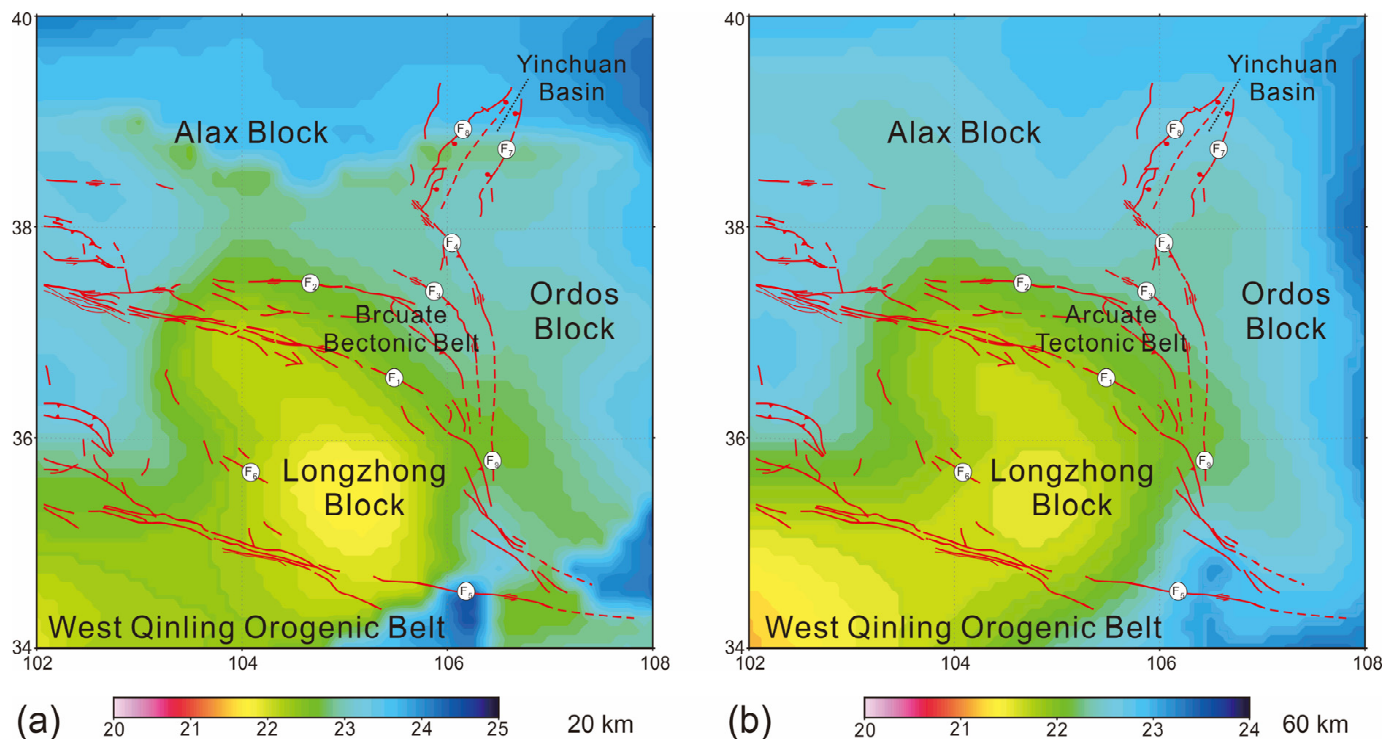


Figure 9. Contour maps of effective viscosity superimposed faults at a depth of 20 km (a), 60 km (b). These two pictures have been modified by CorelDRAW (Version 2018) based on [63]. The lithospheric structure for effective viscosity is according to CRUST 1.0, <http://igppweb.ucsd.edu/~gabi/rem.html> (accessed on 15 July 2013).

Seismic tomography outcomes indicate the presence of low seismic velocity anomalies within the Longzhong block and Yinchuan Basin, which are situated between the Alax block, Ordos block, and the Tibetan Plateau [9,65]. Notably, this low-velocity anomaly zone corresponds to the primary crustal thickening area (Figure 3). The existence of such low-velocity anomalies implies that the rheological strength of the Longzhong block and Yinchuan Basin is likely to be relatively low. This finding is in harmony with the low-strength rheology stipulated in our model (Table 2). Under this particular rheological configuration, the deformation that occurs during the expansion of the plateau is predominantly concentrated within the low-velocity anomaly region and the boundary area between the plateau and the adjacent blocks (Figures 5–7). This observation aligns with the characteristics manifested in the deep crust structure [44,45], where the principal thickening regions of the crust and the abrupt changes in the depth of the Moho are chiefly concentrated at the block boundaries.

Moreover, the findings of this study are consistent with the tectonic deformation evolution process in the studied area. The results demonstrate that the northeastern expansion of the plateau, corresponding to the deformation occurring between 9.5 and 2.5 Ma (Figure 7a), represents the main period for crustal thickening in the northeastern part of the plateau, the Longzhong block, and the Yinchuan Basin. It is also the key period for the formation of the arcuate tectonic belt. Meanwhile, intense shear deformation took place in the southern part of the Alax block and the western part of the Ordos (Figure 6). However, since 2.5 Ma, the direction of compression has shifted from the

northeast to nearly due east, causing the arcuate tectonic belt to exhibit sinistral strike-slip characteristics. Previous investigations into the history of tectonic deformation have revealed that powerful compressive deformation was transmitted northeastward from the Haiyuan fault zone along with the expansion of the plateau. Subsequently, the Xiangshan–Tianjingshan fault zone, Yantongshan fault zone, and Niushoushan–Luoshan fault zone initiated thrust activities one after another, and the arcuate tectonic belt took shape from the end of the late Pliocene to the beginning of the early Pleistocene. At the same time, significant shear deformation occurred at the southern margin of Alax and the western margin of Ordos again [12,25].

The sinistral shear deformation along the southern border of Alax might have instigated the sinistral strike-slip activities in the western segments of the Xiangshan–Tianjingshan and Haiyuan fault zones and the thrust-sinistral strike-slip activities in the eastern part of the Xiangshan–Tianjingshan fault zone. Conversely, the dextral shear deformation along the western margin of Ordos could have triggered dextral strike-slip and thrust activities in the Niushoushan–Luoshan fault zone, Yantongshan fault zone, and the eastern section of the Haiyuan fault zone [12,14,37,66]. Since 2.58 Ma, the direction of the paleotectonic stress field has shifted from NE-SW to ENE-WSW, owing to the continuous resistance of the northern Alax block [14]. The area south of the Xiangshan–Tianjingshan fault zone initiated an eastward movement along the southern edge of the Alax block, exerting pressure on the southern Ordos block. Concurrently, the western parts of the Xiangshan–Tianjingshan and Haiyuan fault zones exhibited significant sinistral strike-slip movements, while the eastern sections were mainly characterized by eastward thrusting. The Yantongshan and Niushoushan–Luoshan fault zones commenced dextral strike-slip and thrust activities, leading to a transformation of the local geomorphic pattern. The four fault zones rotated clockwise and converged towards the Liupanshan tectonic belt, ultimately resulting in the formation of the current arcuate tectonic belt that converges at one end [11]. These deformation histories are in accordance with the deformation process elucidated in this study.

5.2. Formation of the Arcuate Tectonic Belt and the Vertical Heterogeneity in Lithospheric Strength

The lower crustal flow model is often used to explain the lithospheric deformation patterns in the periphery of the Tibetan Plateau, such as the southeastern margin of the Tibetan Plateau [61,67]. The crust and upper mantle structures in the northeastern part of the Tibetan Plateau further imply the existence of low-velocity middle-lower crust in the Longzhong block and the Meso-Cenozoic basins [9,44,45]. However, our findings reveal that a weak middle and lower crust is not essential for the formation of the arcuate tectonic belt. In this model, even when it is assumed that the crustal rheological strength of each block is vertically consistent, the arcuate tectonic belt can still be formed. Its deformation characteristics mainly rely on the lateral heterogeneity of lithospheric strength (Figure 5a–d). Nevertheless, the weak middle and lower crust, functioning as a detachment layer, has contributed to the uplift and thickening of the crust in the Longzhong block and the Meso-Cenozoic basins (Figure 8). This has further promoted the lateral growth of the northeastern margin of the plateau and the formation and expansion of the arcuate tectonic belt. Previous numerical simulation studies have also demonstrated that the lower (or middle-lower) crust with low viscosity and high flow velocity can cause the thickening of the lower (or middle-lower) crust in areas distant from the collision boundary, resulting in surface uplift [28,31,68], which aligns with the outcomes of seismic profile data [69]. Moreover, previous studies have indicated that the arcuate tectonic belt in the northeastern margin of the Tibetan Plateau is a forward-spreading thrust structure based on the detachment layer [21,28,37]. In our model, the weak middle-lower crust of the Longzhong block and

the Meso-Cenozoic basins serves as the detachment layer of the arcuate tectonic belt, which is in accordance with the deep structure characteristics observed through geophysics [9].

5.3. Model Limitation

In this study, a three-dimensional viscous model has been employed to analyze how the heterogeneity of the lithosphere's rheological strength and the alteration of the paleotectonic stress field's direction influence the formation of the arcuate tectonic belt. The results indicate that the lateral heterogeneity of lithosphere strength and the change in the plateau's compression direction are the principal controlling factors for the formation and deformation traits of the arcuate tectonic belt on the northeastern margin of the Tibetan Plateau. Nevertheless, there are certain uncertainties within our numerical model that warrant discussion.

Firstly, our model is a mechanical one based on the viscosity constitutive relation, and it fails to take into account the impact of deep temperature anomalies on viscosity. A free sliding boundary is set at the bottom boundary, which means no deformation occurs in the vertical direction. Such boundary conditions will result in a higher vertical uplift height during the shortening process, and this cannot be compared with the actual terrain. Consequently, the crustal thickness and topography are outcomes of changes relative to the initial model. Additionally, we assigned the same initial crust thickness to each model and did not consider the initial differences in the crust thicknesses of these blocks, which might have an influence on the subsequent deformation process.

Secondly, as we are unaware of the ancient velocity field in the northeastern margin of the Tibetan Plateau, the convergence velocity at the model's boundary is assigned based on the horizontal shortening rate derived from the restored equilibrium profile. This might not align with the complex ancient velocity field. When the model transitions from the thrust stage to the strike-slip stage, the convergent velocity vector on the boundary changes instantaneously, yet, in reality, the actual velocity field may change gradually.

Finally, surface denudation is not taken into account in this study. Surface denudation leads to the redistribution of near-surface materials, which could potentially alter the deformation characteristics of the crust under gravity equilibrium. The uplift of the arcuate mountain systems within the arcuate tectonic belt in the northeastern margin of the Tibetan Plateau is mainly controlled by four main fault zones. The sedimentary strata since the Late Miocene are primarily distributed on both sides of these arcuate mountain systems, suggesting that denudation mainly takes place in the arcuate mountain systems [12]. The thickness of the Ganhegou Formation deposited between approximately 9.5–2.5 Ma ranges from 73 to 752 m, and in the Jingtai area, it is 4671 m, while the thickness of the Yumen Formation deposited after 2.5 Ma is just a few meters [25]. The thin thickness of these deposits indicates that the surface denudation in this area is not intense. Hence, the surface denudation may have a minimal impact on the results of this study.

6. Conclusions

In this paper, a three-dimensional finite element model is employed to explore the formation mechanism of the arcuate tectonic belt in the northeastern margin of the Tibetan Plateau. The following conclusions can be reached:

- (1) The lateral heterogeneity of lithospheric strength in the northeastern margin of the Tibetan Plateau governs the formation of the arcuate tectonic belt. When the lithospheric strength of the Meso-Cenozoic basins is 0.25 times or less than that of the Alax and Ordos blocks, it is more favorable for the formation of the arcuate tectonic belt and the northeastward expansion of the Tibetan Plateau. During the formation

of the arcuate tectonic belt, intense shearing deformation occurs along the southern boundary of the Alax block and the western boundary of the Ordos block.

- (2) The simulation results show that when the viscosity of the middle crust is 10 times that of the lower crust and 0.1 times that of the upper crust, the crust is more conducive to shortening and thickening. The weak middle-lower crust of the Tibetan Plateau is beneficial for the formation of the arcuate tectonic belt and crustal thickening. However, it does not alter the deformation and geomorphology resulting from the horizontal heterogeneity of the lithospheric strength.
- (3) In combination with geological surveys, our results indicate that the arcuate tectonic belt was formed during the NE-SW compression stage from 9.5 to 2.5 Ma. The crustal shortening and thickening propagated from the Haiyuan fault zone to the northeast. Since 2.5 Ma, the faults within the arcuate tectonic belt mainly exhibited strike-slip behavior under the ENE-WSW compression. In the Liupan Shan region, however, the faults showed a nearly E-W orientation with thrust faulting characteristics. Throughout this process, crustal shortening and surface uplift were relatively slight, and the process was primarily characterized by the modification of the geomorphological pattern.

Author Contributions: Conceptualization, W.S., Y.S. and G.H.; Methodology, Y.S.; Software, Y.S.; Validation, Y.S. and G.H.; Formal analysis, W.S., Y.S. and G.H.; Resources, W.S. and Y.S.; Data curation, Y.Z. and Y.S.; Writing—original draft, Y.Z.; Writing—review & editing, W.S., Y.S. and G.H.; Visualization, Y.Z.; Supervision, Y.S.; Funding acquisition, W.S. and Y.S. All authors have read and agreed to the published version of the manuscript.

Funding: This study was funded by research grants from the National Science and Technology Major Project (2024ZD1001102), the National Natural Science Foundation of China (42022029), and the Fundamental Research Funds of CAGS (JKY202419).

Institutional Review Board Statement: Not applicable.

Informed Consent Statement: Not applicable.

Data Availability Statement: Data is contained within the article.

Conflicts of Interest: The authors declare no conflict of interest.

References

1. Molnar, P.; Tapponnier, P. Cenozoic Tectonics of Asia: Effects of a continental collision. *Science* **1975**, *189*, 419–426. [[CrossRef](#)] [[PubMed](#)]
2. Replumaz, A.; Tapponnier, P. Reconstruction of the Deformed Collision Zone between India and Asia by Backward Motion of Lithospheric Blocks. *J. Geophys. Res. Solid Earth* **2003**, *108*, 2285. [[CrossRef](#)]
3. Tapponnier, P.; Peltzer, G.; Armijo, R.; Le Dain, A.-Y.; Cobbold, P. Propagating Extrusion Tectonics in Asia: New Insights from Simple Experiments with Plasticine. *Geology* **1982**, *10*, 611–616. [[CrossRef](#)]
4. Tapponnier, P.; Xu, Z.-Q.; Roger, F.; Meyer, B.; Arnaud, B.N.; Wittlinger, G.; Yang, J.-S. Oblique stepwise rise and growth of the Tibet Plateau. *Science* **2001**, *294*, 1671–1677. [[CrossRef](#)] [[PubMed](#)]
5. Ye, Z.; Li, Q.S.; Gao, R.; Zhang, H.S.; Shen, X.Z.; Liu, X.Z.; Gong, C. Anisotropic Regime across Northeastern Tibet and Its Geodynamic Implications. *Tectonophysics* **2016**, *671*, 1–8. [[CrossRef](#)]
6. Wu, G.-L.; Zhu, C.-Y.; Wang, G.-C.; Zhang, P. Demarcation of the Geomorphological Boundaries of Southeastern Tibet: Implications for Expansion Mechanisms of the Plateau Edge. *Seismol. Geol.* **2019**, *41*, 281–299. (In Chinese with an English Abstract)
7. Molnar, P.; Tapponnier, P. Active Tectonics of Tibet. *J. Geophys. Res. Solid Earth* **1978**, *83*, 5361–5375. [[CrossRef](#)]
8. Tapponnier, P.; Molnar, P. Active Faulting and Tectonics in China. *J. Geophys. Res. Solid Earth* **1977**, *82*, 2905–2930. [[CrossRef](#)]
9. Sun, Q.; Pei, S.-P.; Cui, Z.-X.; Chen, Y.J.; Liu, Y.-B.; Xue, X.-T.; Li, J.-W.; Li, L.; Zuo, H. A New Growth Model of the Northeastern Tibetan Plateau from High-Resolution Seismic Imaging by Improved Double-Difference Tomography. *Tectonophysics* **2021**, *798*, 228699. [[CrossRef](#)]

10. Ma, H.-Y.; Luo, A.-X.; Wang, C.-Y.; Ouyang, Z.-J.; Feng, J.-P. Formation and Evolution Characteristics of Arcuate Tectonic Belt. *J. Xi'an Univ. Sci. Technol.* **2022**, *42*, 752–759. (In Chinese with an English Abstract)
11. Zheng, C.-P.; Li, W.; Xu, S.-Z.; Zhang, J.; Gao, S.-N.; Jia, C. The characteristics and formation mechanism of the curved structural belt. *Chin. J. Geol.* **2018**, *53*, 1171–1185. (In Chinese with an English Abstract) [[CrossRef](#)]
12. Shi, W.; Dong, S.-W.; Liu, Y.; Hu, J.-M.; Chen, X.-H.; Chen, P. Cenozoic Tectonic Evolution of the South Ningxia Region, Northeastern Tibetan Plateau Inferred from New Structural Investigations and Fault Kinematic Analyses. *Tectonophysics* **2015**, *649*, 139–164. [[CrossRef](#)]
13. Dong, X.-P.; Li, Z.-H.; Huang, T.; Jiang, B.-Y.; Cui, J.-W. Origin of the Latent Palaeohigh in Hongsibu Basin of Ningxia, China and Its Effect on the Regional Desertification. *J. Earth Sci. Environ.* **2020**, *42*, 688–700. (In Chinese with an English Abstract) [[CrossRef](#)]
14. Lei, Q.-Y.; Zhang, P.-Z.; Zheng, W.-J.; Chai, C.-Z.; Wang, W.-T.; Du, P.; Yu, J.-X. Dextral Strike-slip of Sanguankou-Niushoushan Fault Zone and Extension of Arc Tectonic Belt in the Northeastern Margin of the Tibet Plateau. *Sci. China Earth Sci.* **2016**, *46*, 691–705. [[CrossRef](#)]
15. Gong, W.-B.; Shi, W.; Chen, H.; Qiu, S.-D.; Yin, Y.-G.; Zhao, Y. Quaternary Active Characteristics of the Liumugao Fault in the Northern Segment of the Niushoushan-Luoshan Fault. *Geol. J.* **2016**, *22*, 1004–1014.
16. Yang, Y.; Qin, X.; Shi, W.; Zhang, Y.; Zhao, Z.-X. Segmentation of the Active Liumugao Fault, NE Tibetan Plateau as Revealed by DEM-derived Geomorphic Indices. *GeoSyst. GeoEnviron.* **2022**, *1*, 100056. [[CrossRef](#)]
17. Chen, H.; Hu, J.-M.; Gong, W.-B.; Kang, R.; Li, L.-B. Characteristics and Transition Mechanism of Late Cenozoic Structural Deformation within the Niushoushan–Luoshan Fault Zone at the Northeastern Margin of the Tibetan Plateau. *J. Asian Earth Sci.* **2015**, *114*, 73–88. [[CrossRef](#)]
18. Li, Y.-C.; Shan, X.-J.; Qu, C.-Y.; Wang, Z.-J. Fault Locking and Slip Rate Deficit of the Haiyuan-Liupanshan Fault Zone in the Northeastern Margin of the Tibetan Plateau. *J. Geodyn.* **2016**, *102*, 47–57. [[CrossRef](#)]
19. Li, X.-N.; Li, C.-Y.; Pierce, I.K.D.; Zhang, P.-Z.; Zheng, W.-J.; Dong, J.-Y.; Chen, G.; Ai, M.; Ren, G.-X.; Luo, Q.-X. New Slip Rates for the Tianjingshan Fault Using Optically Stimulated Luminescence, GPS, and Paleoseismic Data, NE Tibet, China. *Tectonophysics* **2019**, *755*, 64–74. [[CrossRef](#)]
20. Tian, Q.-J.; Ding, G.-Y. The Tectonic Feature of a Quasi-trijunction in the Northeastern Corner of Qinghai-Xizang Plateau. *Earthq. Res. China* **1998**, *14*, 27–35. (In Chinese with an English Abstract)
21. Wang, W.-T.; Zhang, P.-Z.; Lei, Q.-Y. Deformational Characteristics of the Niushoushan-Luoshan Fault Zone and Its Tectonic Implications. *Seismol. Geol.* **2013**, *35*, 195–207. (In Chinese with an English Abstract) [[CrossRef](#)]
22. Chen, Q.-Z.; Hu, C.-B.; Orellana-Rovirosa, F.; Zhang, K.-J.; Zhou, L.-S.; Zhang, H.; Shi, Y.-L. Geodynamics of Progressive Growth of Arcuate Fold-and-Thrust Belts: Insights from Numerical Modeling of the NE Margin of the Qinghai-Tibetan Plateau. *J. Struct. Geol.* **2023**, *175*, 104939. [[CrossRef](#)]
23. Wang, T.-Y.; Shi, W.; Hou, G.-T.; Wang, J.-Q.; Li, Z.-C.; Zhao, Y.-L. Neogene Paleomagnetic Chronology of the Laolongwan Basin, NW China: New Insight for the Northeastward Expansion of the Tibetan Plateau. *J. Asian Earth Sci.* **2024**, *265*, 106115. [[CrossRef](#)]
24. Zhao, Z.-X.; Shi, W.; Yang, Y. Late Cenozoic Geomorphic Evolution in the Northeastern Tibetan Plateau: Constraints on U-Pb Age Spectra of Detrital Zircons in the Wuwei Basin, NW China. *Geomorphology* **2024**, *449*, 109044. [[CrossRef](#)]
25. Shi, W.; Hu, J.-M.; Chen, P.; Chen, H.; Wang, Y.-C.; Qin, X.; Zhang, Y.; Yang, Y. Yumen Conglomerate Ages in the South Ningxia Basin, North-eastern Tibetan Plateau, as Constrained by Cosmogenic Dating. *Geol. J.* **2020**, *55*, 7138–7147. [[CrossRef](#)]
26. Burov, E.B. Rheology and Strength of the Lithosphere. *Mar. Pet. Geol.* **2011**, *28*, 1402–1443. [[CrossRef](#)]
27. Liu, M.; Yang, Y.-Q. Extensional Collapse of the Tibetan Plateau: Results of Three-dimensional Finite Element Modeling. *J. Geophys. Res. Solid Earth* **2003**, *108*, 2361. [[CrossRef](#)]
28. Meissner, R.; Mooney, W. Weakness of the Lower Continental Crust: A Condition for Delamination, Uplift, and Escape. *Tectonophysics* **1998**, *296*, 47–60. [[CrossRef](#)]
29. Zang, S.X.; Wei, R.Q.; Liu, Y.G. Three-dimensional rheological structure of the lithosphere in the Ordos and its adjacent area. *Geophys. J. Int.* **2005**, *163*, 339–356. [[CrossRef](#)]
30. Zang, S.X.; Wei, R.-Q.; Ning, J.-Y. Effect of the Brittle Fracture on the Rheological Structure of the Lithosphere and Its Applications in the Ordos. *Tectonophysics* **2007**, *429*, 267–285. [[CrossRef](#)]
31. Zhao, W.-L.; Morgan, W.J. Injection of Indian Crust into Tibetan Lower Crust. *Tectonics* **1987**, *6*, 489–504. [[CrossRef](#)]
32. Shi, W.; Dong, S.-W.; Hu, J.-M. Neotectonics around the Ordos Block, North China: A Review and New Insights. *Earth-Sci. Rev.* **2020**, *200*, 102969. [[CrossRef](#)]
33. Li, Y.-C.; Shan, X.-J.; Qu, C.-Y.; Zhang, Y.-F.; Song, X.-G.; Jiang, Y.; Zhang, G.-H.; Nocquet, J.-M.; Gong, W.-Y.; Gan, W.-J.; et al. Elastic Block and Strain Modeling of GPS Data around the HaiyuanLiupanshan Fault, Northeastern Tibetan Plateau. *J. Asian Earth Sci.* **2017**, *150*, 87–97. [[CrossRef](#)]
34. Shi, F.; He, H.-L.; Gao, W.; Sun, H.-Y.; Wei, Z.-Y.; Hao, H.-J.; Zou, J.-J.; Sun, W.; Su, P. Holocene Paleearthquakes on the Tianqiaogou-Huangyangchuan Fault in the Northeastern Boundary Fault System of the Tibetan Plateau. *J. Asian Earth Sci.* **2019**, *186*, 104049. [[CrossRef](#)]

35. Lu, H.-F.; Chen, H.-L.; Yang, Y.; Zhang, J.-Z. Activities and Geomorphic Deformation of the Fault Belt on the Southern Margin of Wuwei Basin, Gansu Province during the Late Quaternary. *Geol. Bull. China* **2022**, *41*, 327–346. (In Chinese with an English Abstract)
36. Zhan, Y.; Zhao, G.-Z.; Wang, J.-J.; Tang, J.; Chen, X.-B.; Deng, Q.-H.; Xuan, F.; Zhao, J.-M. Crustal Electric Structure of Haiyuan Arcuate Tectonic Region in the Northeastern Margin of Qinghai-Xizang Plateau, China. *Acta Seismol. Sin.* **2005**, *27*, 431–440. (In Chinese with an English Abstract) [[CrossRef](#)]
37. Yuan, Z.-Z.; Lin, Y.-Q.; Xu, X.; Li, H.-L.; Guo, X.-Y.; Li, C.-S.; Tong, X.-F. Crustal-scale Architecture and Origin of the Haiyuan Arcuate Tectonic Belt, NE Tibet. *Tectonophysics* **2024**, *890*, 230485. [[CrossRef](#)]
38. Song, X.-H.; Pan, S.-Z.; Wang, F.-Y.; Tian, X.-F.; Liu, B.-F.; Song, J.-J. Deep Crustal Structure and Deformation Features of the Northeastern Margin of the Tibetan Plateau, as Revealed by Controlled-source Seismic Profiling along the Aba-Guyuan-Wuqi Transect. *Tectonophysics* **2024**, *885*, 230418. [[CrossRef](#)]
39. Chen, H.; Hu, J.-M.; Gong, W.-B.; Li, L.-B. Cenozoic Deformation and Evolution of the Niushou Shan-Luo Shan Fault Zone in the Northeast Margin of the Tibet Plateau. *Earth Sci. Front.* **2013**, *20*, 18–35. (In Chinese with an English Abstract)
40. Laske, G.; Masters, G.; Ma, Z.-T.; Pasyanos, M.E. Update on CRUST1.0: A 1-degree Global Model of Earth's Crust. *Geophys. Res. Abstr.* **2013**, *15*, 2658.
41. Walter, D.M.; Carol, B.-L.; María, G.S.; Miguel, A.C. Earth Crustal Model 1(ECM1): A $1^\circ \times 1^\circ$ Global Seismic and Density Model. *Earth-Sci. Rev.* **2023**, *243*, 104493. [[CrossRef](#)]
42. Chen, Y.-F.; Chen, J.-H.; Guo, B.; Li, S.-C.; Li, Y.; Qi, S.-H.; Zhao, P.-P. Seismic Structure and Deformation Features beneath the Yinchuan-Hetao Graben, NW China. *Phys. Earth Planet. Inter.* **2022**, 329–330, 106911. [[CrossRef](#)]
43. Liu, B.-J.; Feng, S.-Y.; Ji, J.-F.; Wang, S.-J.; Zhang, J.-S.; Yuan, H.-K.; Yang, G.-J. Lithospheric Structure and Faulting Characteristics of the Helan Mountains and Yinchuan Basin: Results of Deep Seismic Reflection Profiling. *Sci. China Earth Sci.* **2017**, *60*, 589–601. [[CrossRef](#)]
44. Wang, S.-J.; Liu, B.-J.; Jia, S.-X.; Deng, X.-G.; Song, X.-H.; Li, Y.-Q. Study on S-wave Velocity Structure Difference of Yinchuan Basin and Blocks on Both Sides Using Artificial Seismic Sounding Profiles. *Prog. Geophys.* **2017**, *32*, 1936–1943. (In Chinese with an English Abstract) [[CrossRef](#)]
45. Tian, X.-B.; Bai, Z.-M.; Klemperer, S.L.; Liang, X.-F.; Liu, Z.; Wang, X.; Yang, X.-S.; Wei, Y.-H.; Zhu, G.-H. Crustal-Scale Wedge Tectonics at the Narrow Boundary between the Tibetan Plateau and Ordos Block. *Earth Planet. Sci. Lett.* **2021**, *554*, 116700. [[CrossRef](#)]
46. Wang, S.-J.; Liu, B.-J.; Tian, X.-F.; Liu, B.-F.; Song, X.-H.; Deng, X.-G.; Sun, Y.-N.; Ma, C.-J.; Yang, Y.-D. Crustal P-wave Velocity Structure in the Northeastern Margin of the Qinghai-Tibetan Plateau and Insights into Crustal Deformation. *Sci. China Earth Sci.* **2019**, *61*, 1221–1237. [[CrossRef](#)]
47. Zhang, Z.-J.; Bai, Z.-M.; Klemperer, S.L.; Tian, X.-B.; Xu, T.; Chen, Y.; Teng, J.-W. Crustal Structure across Northeastern Tibet from Wide-Angle Seismic Profiling: Constraints on the Caledonian Qilian Orogeny and Its Reactivation. *Tectonophysics* **2013**, *606*, 140–159. [[CrossRef](#)]
48. Coblenz, D.D.; Richardson, R.M. Analysis of the South American Intraplate Stress Field. *J. Geophys. Res. Solid Earth* **1996**, *101*, 8643–8657. [[CrossRef](#)]
49. Richardson, R.M. Finite Element Modeling of Stress in the Nazca Plate: Driving Forces and Plate Boundary Earthquakes. *Tectonophysics* **1978**, *50*, 223–248. [[CrossRef](#)]
50. Clark, M.K.; Bush, J.W.M.; Royden, L.H. Dynamic Topography Produced by Lower Crustal Flow against Rheological Strength Heterogeneities Bordering the Tibetan Plateau. *Geophys. J. Int.* **2005**, *162*, 575–590. [[CrossRef](#)]
51. Cook, K.L.; Royden, L.H. The Role of Crustal Strength Variations in Shaping Orogenic Plateaus, with Application to Tibet. *J. Geophys. Res. Solid Earth* **2008**, *113*, B08407. [[CrossRef](#)]
52. England, P.; Houseman, G. Finite Strain Calculations of Continental Deformation 2. Comparison with the India–Asia Collision Zone. *J. Geophys. Res. Solid Earth* **1986**, *91*, 3664–3676. [[CrossRef](#)]
53. England, P.; McKenzie, D. A Thin Viscous Sheet Model for Continental Deformation. *Geophys. J. R. Astron. Soc.* **1986**, *70*, 295–321. [[CrossRef](#)]
54. Houseman, G.; England, P. Finite Strain Calculations of Continental Deformation 1. Method and General Results for Convergent Zones. *J. Geophys. Res. Solid Earth* **1986**, *91*, 3651–3663. [[CrossRef](#)]
55. Royden, L.H.; Burchfiel, B.C.; King, R.W.; Wang, E.; Chen, Z.-L.; Shen, F.; Liu, Y.-P. Surface Deformation and Lower Crustal Flow in Eastern Tibet. *Science* **1997**, *276*, 788–790. [[CrossRef](#)] [[PubMed](#)]
56. Sun, Y.-J.; Dong, S.-W.; Zhang, H.; Shi, Y.-L. Numerical Investigation of the Geodynamic Mechanism for the Late Jurassic Deformation of the Ordos Block and Surrounding Orogenic Belts. *J. Asian Earth Sci.* **2015**, *114*, 623–633. [[CrossRef](#)]
57. Buitter, S.J.H.; Babeyko, A.Y.; Ellis, S.; Gerya, T.V.; Kaus, B.J.P.; Kellner, A.; Schreurs, G.; Yamada, Y. The Numerical Sandbox: Comparison of Model Results for a Shortening and an Extension Experiment. *Geol. Soc. Lond. Spec. Publ.* **2006**, *253*, 29–64. [[CrossRef](#)]

58. Gerya, T.V.; Yuen, D.A. Characteristics-Based Marker-in-Cell Method with Conservative Finite-Differences Schemes for Modeling Geological Flows with Strongly Variable Transport Properties. *Phys. Earth Planet. Inter.* **2003**, *140*, 293–318. [[CrossRef](#)]
59. Sun, Y.-J.; Liu, M. Edge-Driven Asthenospheric Convection beneath the North China Craton: A Numerical Study. *Tectonophysics* **2023**, *849*, 229726. [[CrossRef](#)]
60. Xu, X.-M.; Niu, F.-L.; Ding, Z.-F.; Chen, Q.-F. Complicated Crustal Deformation beneath the NE Margin of the Tibetan Plateau and Its Adjacent Areas Revealed by Multi-station Receiver-function Gathering. *Earth Planet. Sci. Lett.* **2018**, *497*, 204–216. [[CrossRef](#)]
61. Royden, L.H.; Burchfiel, B.C.; Robert, D.V.D.H. The Geological Evolution of the Tibetan Plateau. *Science* **2008**, *321*, 1054–1058. [[CrossRef](#)]
62. Sun, Y.-J.; Liu, M. Rheological control of lateral growth of the Tibetan Plateau: Numerical results. *J. Geophys. Res. Solid Earth* **2018**, *123*, 10124–10141. [[CrossRef](#)]
63. Sun, Y.-J.; Dong, S.-W.; Liu, M.; Zhang, H.; Shi, Y.-L. The Rheological Structure of East Asian Continental Lithosphere. *Tectonophysics* **2025**, *895*, 230575. [[CrossRef](#)]
64. Lucazeau, F. Analysis and mapping of an updated terrestrial heat flow data set. *Geochem. Geophys. Geo Syst.* **2019**, *20*, 4001–4024. [[CrossRef](#)]
65. Li, H.-L.; Ye, Z.; Gao, R.; Huang, X.-F. A Distinct Contrast in the Lithospheric Structure and Limited Crustal Flow across the Northeastern Tibetan Plateau: Evidence from Vs and Vp/Vs Imaging. *Tectonophysics* **2022**, *836*, 229413. [[CrossRef](#)]
66. Li, X.-N.; Li, C.-Y.; Zhang, P.-Z.; Wang, X.-G.; Zhang, L.-S. Changes in Fault Movement Property and Genetic Mechanism on the Western Segment of the Xiangshan-Tianjingshan Fault Zone. *Seismol. Geol.* **2016**, *38*, 732–746. (In Chinese with an English Abstract) [[CrossRef](#)]
67. Clark, M.K.; Royden, L.H. Topographic Ooze: Building the Eastern Margin of Tibet by Lower Crustal Flow. *Geology* **2000**, *28*, 703–706. [[CrossRef](#)]
68. Sun, Y.-J.; Hu, D.-G.; Zhang, H.; Fan, T.-Y.; Zhang, Y.-L.; Li, B.; Shi, Y.-L. Numerical Study on the Dynamics of Lithospheric Deformation Pattern in the Northeastern Tibetan plateau. *Prog. Geophys.* **2017**, *32*, 2383–2393. (In Chinese with an English Abstract) [[CrossRef](#)]
69. Liu, M.-J.; Mooney, W.D.; Li, S.-L.; Okaya, N.; Detweiler, S. Crustal Structure of the Northeastern Margin of the Tibetan Plateau from the Songpan-Ganzi Terrane to the Ordos Basin. *Tectonophysics* **2006**, *420*, 253–266. [[CrossRef](#)]

Disclaimer/Publisher’s Note: The statements, opinions and data contained in all publications are solely those of the individual author(s) and contributor(s) and not of MDPI and/or the editor(s). MDPI and/or the editor(s) disclaim responsibility for any injury to people or property resulting from any ideas, methods, instructions or products referred to in the content.